

# Complex Spatiotemporal Antiphase Oscillations during Electrodeposition of a Metal Disk Electrode: Model Calculations

Adrian Bîrzu,<sup>†,‡</sup> Florian Plenge,<sup>‡</sup> Nils I. Jaeger,<sup>§</sup> John L. Hudson,<sup>||</sup> and Katharina Krischer<sup>\*,†,‡</sup>

Department of Physics, Technical University of München, James-Frank-Strasse 1, 85748 Garching, Germany, Fritz Haber Institute of the Max Planck Society, Faradayweg 4-6, 14195 Berlin, Germany, Institute for Applied and Physical Chemistry, University of Bremen, FB 2-Biology/Chemistry, Postfach 330 440, 28334 Bremen, Germany, and Department of Chemical Engineering, 102 Engineers' Way, University of Virginia, Charlottesville, Virginia 22904-4741

Received: November 20, 2002; In Final Form: February 19, 2003

Pattern formation in electrochemical systems depends sensitively on the relative arrangement of the electrodes. We present simulations of spatiotemporal patterns during the electrodeposition of a metal disk electrode in which the reference electrode is located on the axis of the disk and close to the metal working electrode. This geometry introduces a strong but asymmetric negative feedback which tends to destabilize the homogeneous potential distribution. We demonstrate that the feedback gives rise to a variety of complex antiphase-type patterns. Some of these patterns have been observed in experiments; others present novel manifestations of dynamic instabilities in electrochemical systems.

## 1. Introduction

It is well-known that electrochemical systems often undergo oscillatory instabilities, resulting in macroscopic oscillations of the total current and the average electrode potential.<sup>1–3</sup> More recent experimental<sup>4–22</sup> and theoretical<sup>23–34</sup> studies revealed that the oscillations are often not homogeneous but are accompanied by the formation of spatial patterns. A peculiar property of electrochemical pattern formation is its sensitive dependence on the precise geometry of the cell, in particular on the relative positions of the electrodes (see, e.g., the review articles in refs 35 and 36). This follows from the fact that in electrochemical systems the dominant spatial coupling along the electrode is through the electric field in the electrolyte. Suppose the potential distribution at the double layer changes locally, e.g., due to a local fluctuation. Then, the potential distribution in the entire electrolyte will adjust and thus also the double-layer potential distribution at the interface. Hence, different positions along the electrode are coupled together through the electric field. This type of coupling has been termed “migration coupling”.<sup>33,35,36</sup> For given electrode potentials, the forms, sizes, and positions of the working (WE) and the counter (CE) electrodes mainly determine the electric potential distribution through the electrolyte, and therefore, the spatial coupling can be tuned by varying, e.g., the distance between the WE and the CE.<sup>25</sup> A metal/insulator transition in the plane of the WE, such as that in the case of disk electrodes, further complicates the situation because it excludes the existence of strictly homogeneous states.<sup>33,36</sup> Rather, the metal–insulator transition causes the homogeneous dynamics as well as the migration coupling to depend on space.

In addition, the potentiostatic control in a three electrode setup introduces a feedback into the system which can alter the

stability of the states and the pattern formation drastically.<sup>19,29–32,37–39</sup> The origin of this feedback becomes plausible keeping in mind that a *local* change of the electrode potential causes a redistribution of the electric potential throughout the electrolyte, i.e., also at the position at which the RE probes the electrolyte potential (e.g., at the tip of a Haber–Luggin capillary). Hence, the actual and the set potential difference between the WE and the RE differ, and the potentiostat changes the Galvani potential of the WE (or, equivalently, of the CE) such that the potentiostatic constraint ( $U = \phi_{DL} + IR$ , where  $U$  is the set voltage,  $\phi_{DL}$  the electrode potential, and  $IR$  the potential drop through the electrolyte between the WE and the RE) is again fulfilled. Obviously, this feedback affects all positions of the WE. In this respect, it is a global feedback. However, defining a global feedback in a more strict sense, namely, that the local dynamics depends on the *average* of a system's variable, a global coupling through the potentiostatic control is realized only in cases in which every point on the WE has the same distance to the RE. This is only fulfilled for (quasi-one-dimensional) ring electrodes if the RE is located on the axis of the ring. In this case, bringing the RE closer to the WE is identical in terms of the dynamics to inserting a negative Ohmic resistor in series to the WE.<sup>40</sup> In all other cases and, in particular, for all two-dimensional electrodes, and hence also for the disk electrodes considered in this paper, the feedback depends on a weighted average of the electrode potential. For simplicity we will use the term “global coupling” also in this situation. Thus, we do not use it in the strict sense but include this more general type of feedback.

Analyzing the effect of the global feedback on the local evolution of the electrode potential, it was shown that the feedback drives the electrode potential at every position away from the average electrode potential, i.e., if the local potential value is larger than the average electrode potential, it is driven to still larger values, and if it is smaller, it becomes even smaller due to the global coupling (see, e.g., the review article in ref 36). Such a global coupling is called a negative global coupling. It tends to favor the formation of patterns.

\* Corresponding author. E-mail: krischer@ph.tum.de.

<sup>†</sup> Technical University of München.

<sup>‡</sup> Fritz-Haber Institute of the Max Planck Society.

<sup>§</sup> University of Bremen.

<sup>||</sup> University of Virginia.

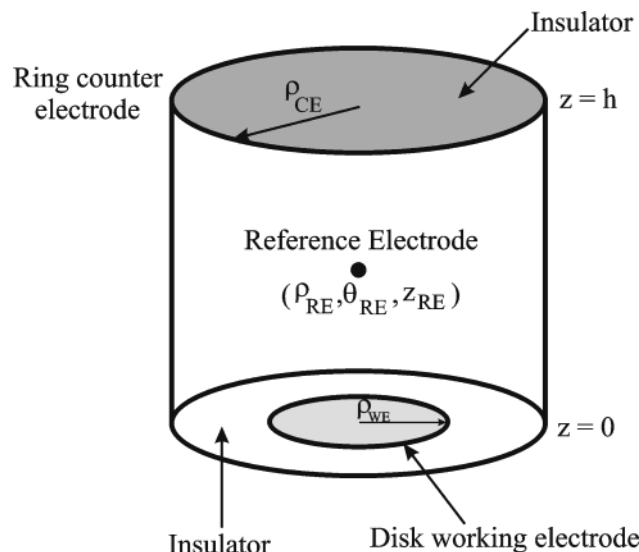


**Figure 1.** Geometry of the electrochemical cell.

In this paper we are considering pattern formation on disk electrodes with the RE on an axisymmetrical position and close to the WE. This gives rise to a strong negative global coupling. The employed model is a generic model describing electrodis-solution of metals that exhibit an active–passive transition. Some of the patterns obtained have been observed experimentally during Fe dissolution,<sup>5,21</sup> the presented simulations elucidating at least some features of the underlying instability.

## 2. The Model

Many metals exhibit an active (high current)–passive (low current) transition when increasing the electrode potential, giving rise to a region of negative differential resistance (NDR) in the current–potential characteristic. Under appropriate conditions, the NDR leads to the onset of dynamic instabilities and the system exhibits oscillations or bistability.<sup>3,36</sup> The model we use here qualitatively describes the dynamics of such metals under potentiostatic control. It is based on the original idea by Franck and FitzHugh that the transition potential is a function of the pH in front of the electrode, which, in turn, varies as the migration current density varies. The reaction kinetics was described using a smoothed Heaviside function.<sup>41</sup> Thus, the main variables of the model are proton concentration in front of the electrode and the potential drop across the double layer of the working electrode. Changes of the latter, however, depend on the entire electric potential distribution in the electrochemical cell,  $\phi(\rho, \theta, z)$ , which, thus, also has to be calculated. Clearly, the latter depends on the geometry of the cell.

The geometry of the electrochemical cell implemented in the model is shown in Figure 1. The cell is a cylinder with radius  $\rho_{CE}$  and height  $h$ . Its walls are insulating, except at the positions of the working electrode (WE) and the counter electrode (CE). The metal disk working electrode (WE) of radius  $\rho_{WE}$  is located axial-symmetrically at the bottom of the cylinder. The counter electrode is a ring of radius  $\rho_{CE}$ , situated coaxially above the working electrode, at a vertical distance  $h$ , i.e., at the “top” of the cell. The reference electrode is placed on the cell’s axis at various distances from the WE.

A detailed presentation of the model equations is given in previous papers;<sup>29,31</sup> thus, here we introduce them only briefly.

The bulk electrolyte is supposed to be strictly electroneutral, and thus,  $\phi$  has to satisfy Laplace’s equation (for a discussion of strict electroneutrality, see Newman<sup>42</sup>):

$$\nabla^2 \phi = 0 \quad (1)$$

where  $\phi(\rho, \theta, z)$  is the potential at a given location in the electrolyte.

At the insulating cell walls,

$$\left. \frac{\partial \phi}{\partial \rho} \right|_{\rho=\rho_{CE}, \theta, 0 < z < h} = 0; \quad \left. \frac{\partial \phi}{\partial z} \right|_{\rho_{WE} < \rho < \rho_{CE}, \theta, z=0} = 0; \quad \left. \frac{\partial \phi}{\partial z} \right|_{0 \leq \rho < \rho_{CE}, \theta, z=h} = 0 \quad (2)$$

At the counter electrode, linear kinetics is assumed and the capacitive current is neglected:

$$-\sigma \left. \frac{\partial \phi}{\partial z} \right|_{CE} = k(\phi|_{CE} - \phi_{metal}^{CE}) \quad (3)$$

Here,  $\sigma$  is the electrical conductivity of the electrolyte,  $k$  a rate constant in [ $\Omega^{-1} \text{ m}^{-2}$ ], and  $\phi_{metal}^{CE}$  is the homogeneous potential of the metal of the counter electrode (Galvani potential). Note that  $\phi_{metal}^{CE}$  adapts such that the potentiostatic constraint is satisfied at any time. Thus,  $\phi_{metal}^{CE}$  can vary in time. The difference  $\phi|_{CE} - \phi_{metal}^{CE}$  is thus the potential drop across the electrical double layer in front of the counter electrode.

Due to the potentiostatic control, the applied voltage between the pointlike reference electrode and the metal of the working electrode (taken as reference)  $E_{apl}$  is constant:

$$\phi(\rho_{RE}, \theta_{RE}, z_{RE}) = E_{apl} \quad \text{with} \quad \phi_{metal}^{WE} = 0 \quad (4)$$

With this definition of the reference potential, the potential close to the working electrode  $\phi|_{WE}$  and the potential drop over the electrical double layer in front of the working electrode are related by the equation

$$\phi|_{WE} = -\phi_{DL} \quad (5)$$

At the working electrode, the local migration current density is the sum of capacitive and reaction current densities:

$$\sigma \left. \frac{\partial \phi}{\partial z} \right|_{WE} = -i_{cap} - i_{reac} = C_{dl} \left. \frac{\partial \phi}{\partial t} \right|_{WE} - \frac{A}{e^{-\alpha(-\phi_{DL} + E_f([H_{WE}^+]))} + 1} \quad (6)$$

$C_{dl}$  is the specific capacitance of the double layer,  $A$  is a constant giving the amplitude of the reaction current density,  $\alpha \gg 1$  determines the steepness of the smoothed Heaviside function which models the reaction current, and  $[H_{WE}^+]$  is the concentration of hydrogen ions at the working electrode. Hence, it is assumed that all quantities determining the reaction current except of  $[H_{WE}^+]$  instantaneously adjust to their equilibrium values upon changes of  $[\phi_{DL}]$ .

The active–passive transition potential (the Flade potential)  $E_f$  is assumed to be a linear function of the pH in front of the working electrode:

$$E_f([H_{WE}^+]) = F_1 + F_2 \log([H_{WE}^+]) \quad (7)$$

The concentration of hydrogen ions in the bulk solution is assumed to be constant  $[H_{bulk}^+]$ , and in front of the working electrode,  $[H_{WE}^+]$  is assumed to change due to diffusion and migration (i.e., we assume that Faradaic contributions can be neglected):

$$\frac{\partial[\text{H}_{\text{WE}}^+]}{\partial t} = \frac{2D([\text{H}_{\text{bulk}}^+] - [\text{H}_{\text{WE}}^+])}{\delta^2} + \frac{2F\mu[\text{H}_{\text{WE}}^+]}{\delta} \frac{\partial\phi}{\partial z}\bigg|_{\text{WE}} \quad (8)$$

where  $D$  and  $\mu$  are the diffusion coefficient and the mobility of the protons, respectively,  $F$  is the Faraday constant, and  $\delta$  is the thickness of the diffusion layer in front of the working electrode. For the concentration profile perpendicular to the electrode in the diffusion layer, a linear approximation has been made.<sup>43</sup>

We used the following transformations to obtain dimensionless quantities:

- the dimensionless time,

$$t' = \frac{2D}{\delta^2} t \quad (9a)$$

- the dimensionless vertical coordinate,

$$z' = \frac{z}{h} \quad (9b)$$

- the dimensionless radial coordinate,

$$\rho' = \frac{\rho}{\rho_{\text{WE}}} \quad (9c)$$

- the dimensionless proton concentration,

$$[\text{H}_{\text{WE}}^+] = \frac{[\text{H}_{\text{WE}}^+]}{[\text{H}_{\text{bulk}}^+]} \quad (9d)$$

- the dimensionless potential and the applied voltage,

$$\phi' = \frac{F}{RT}\phi; \quad V_{\text{apl}} = \frac{F}{RT}E_{\text{apl}} \quad (9e)$$

where  $R$  is the gas constant and  $T$  the absolute temperature,

- the dimensionless reaction current,

$$i'_{\text{reac}} = \frac{i_{\text{reac}}}{A_0}$$

with

$$A_0 = 1 \text{ mA/cm}^2 \quad (9f)$$

With eq 9a–f, the eqs 6 and 8 evolve into (omitting the primes for clarity):

$$\epsilon \frac{\partial\phi}{\partial t}\bigg|_{\text{WE}} = \sigma^* \frac{\partial\phi}{\partial z}\bigg|_{\text{WE}} + i_{\text{reac}}(\phi, [\text{H}_{\text{WE}}^+]) \quad (10a)$$

$$\frac{\partial[\text{H}_{\text{WE}}^+]}{\partial t} = (1 - [\text{H}_{\text{WE}}^+]) + \gamma[\text{H}_{\text{WE}}^+] \frac{\partial\phi}{\partial z}\bigg|_{\text{WE}} \quad (10b)$$

where

$$\epsilon = \frac{2DC_{\text{dl}}}{\delta^2 A} \frac{RT}{F}; \quad \sigma^* = \frac{\sigma}{hA} \frac{RT}{F}; \quad \gamma = \frac{\mu\delta RT}{Dh}$$

**Numerical Aspects.** Laplace's equation in cylindrical coordinates and dimensionless variables is given by

$$\frac{\partial^2\phi}{\partial\rho^2} + \frac{1}{\rho} \frac{\partial\phi}{\partial\rho} + \frac{1}{\rho^2} \frac{\partial^2\phi}{\partial\theta^2} + \left(\frac{\rho_{\text{WE}}}{h}\right)^2 \frac{\partial^2\phi}{\partial z^2} = 0 \quad (11)$$

The discrete form of this equation was obtained using a space-centered finite-difference method on a cylindrical grid.<sup>44</sup> Usually between 20 and 40 grid points were used along each space direction.

Equation 11 together with the dimensionless form of the boundary conditions 2–5 and eq 10a,b determines the potential distribution in the electrolyte at any moment. The dimensionless form of the boundary condition at the counter electrode is

$$\frac{\partial\phi}{\partial z}\bigg|_{\text{CE}} = -\frac{kh}{\sigma}(\phi|_{\text{CE}} - \phi_{\text{metal}}^{\text{CE}}) \quad (12)$$

This equation introduces an additional unknown,  $\phi_{\text{metal}}^{\text{CE}}$ . Nevertheless, the boundary value problem is well-posed, because at the reference electrode both Laplace's equation and the potentiostatic control condition

$$\phi|_{\text{RE}} = V_{\text{apl}} \quad (13)$$

are satisfied.

Among the boundary conditions, eq 10a,b is special, as it is time-dependent. The integration in time for this evolving boundary condition was done using a fourth-order Runge–Kutta method. The gradient of the potential in front of the working electrode appears in the right-hand side of eq 10a. It is obtained from the solution of Laplace's equation, which, consequently, has to be solved at each time integration step.

The linear algebraic system obtained from Laplace's equation and the boundary conditions was solved using the ma48 routines from the HSL 2002 library.<sup>45</sup>

### 3. Results and Discussion

**3.1. Base Antiphase Oscillations.** An outstanding experimental example of pattern formation during metal dissolution reaction was the observation of a period-doubled oscillatory state, whereby during each oscillation of the global current only half of the electrode seemed to undergo the oscillatory cycle whereas the second half remained apparently in the passive state.<sup>5</sup>

As already mentioned in a previous paper,<sup>31</sup> a similar behavior could be found in our simulations, and in fact, it represents the most frequently observed spatiotemporal behavior if the RE is located close to the WE. Figure 2 displays an example of such an antiphase oscillation. Figure 2a shows the evolution of the electrode potential as a function of time and angular coordinate for a fixed, intermediate radial position on the working electrode. Red denotes an active region and blue a passive one. When half of the electrode is active, the opposite half is passive, the situation alternating in time.

Figure 2b shows the potential distribution on the disk at different moments in time during one oscillation period. In the initial frame, approximately half of the disk is active. The amplitude of the active region starts to decrease (frames 2 and 3), leaving a low-amplitude active region, which travels to the opposite part of the disk (frames 4 and 5), where the amplitude grows again to its maximum value (frames 6 and 7). Similar transformations bring the system back to its initial state during the second half of the oscillation period. The two-half cycles are symmetric with respect to a rotation by 180° and a shift of half an oscillation period in time. Consequently, the global current exhibits a simple periodic oscillation with half the period of a local time series. Two locations on the electrode surface

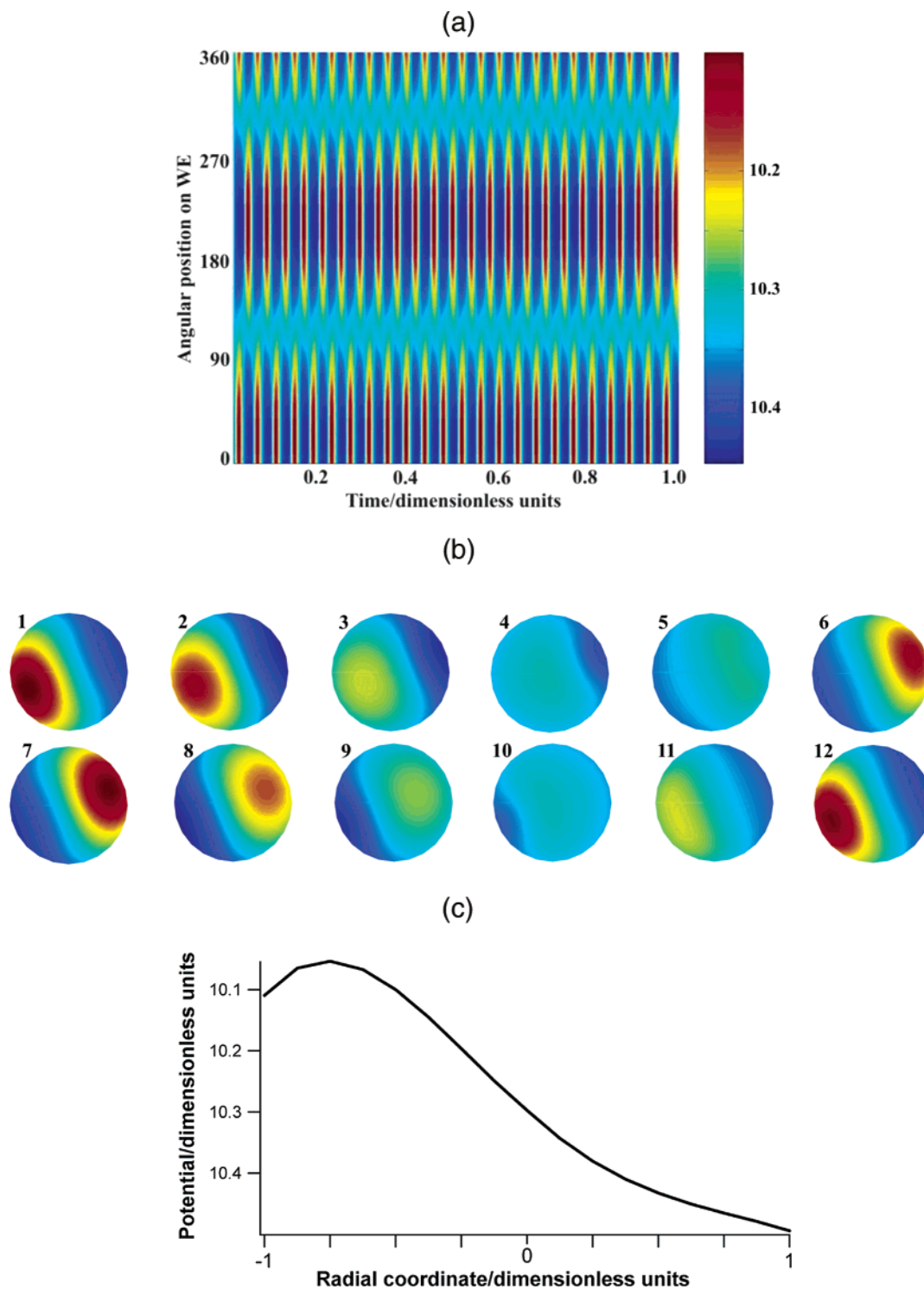


**Figure 2.** “Base” antiphase oscillations. (a) Potential drop across the double layer as a function of angular position on the disk at  $\rho = 0.5\rho_{WE}$  and time. The color bar shows the coding of the dimensionless electrode potential: blue represents passive and red, active. (b) Snapshots of the potential on the disk working electrode at different times during one oscillation period. Note that the color scale is slightly different than the one shown in (a). (c) Profile of the electrode potential as a function of the radius at the angle of the symmetry plane corresponding to snapshot 1 in (b). Parameter values:  $\epsilon = 1.03 \times 10^{-2}$ ,  $\sigma^* = 0.155$ ,  $\gamma = 0.258$ ,  $V_{apl} = -10.446$ ,  $\alpha = 6.46$ ,  $F_1 = 46.43$ ,  $F_2 = 464.27$ ,  $(h/\rho_{CE}) = 1.57$ ,  $z_{RE} = 0.2$ , and  $(\rho_{WE}/\rho_{CE}) = 0.8$ .

that are transformed into each other by the above-mentioned symmetry operation oscillate  $180^\circ$  out of phase, which led to the notation “antiphase oscillations”. Since we observed different dynamics that bifurcate from this state, below we refer to it also as the “base state” or the “base oscillation”. With respect to the global behavior, which repeats itself after half a local oscillation period, the dynamics is spatiotemporally period doubled.

Two observations should be stressed here. First, the antiphase oscillations were obtained only if the RE was sufficiently close to the WE (in our case at one-fifth of the distance between WE and CE), i.e., in the presence of a strong negative global coupling. Second, the radial profiles of the potential distribution are strongly influenced by the insulator surrounding the disk electrode. It is known that the potential distribution at a disk electrode is never completely uniform owing to the mixed



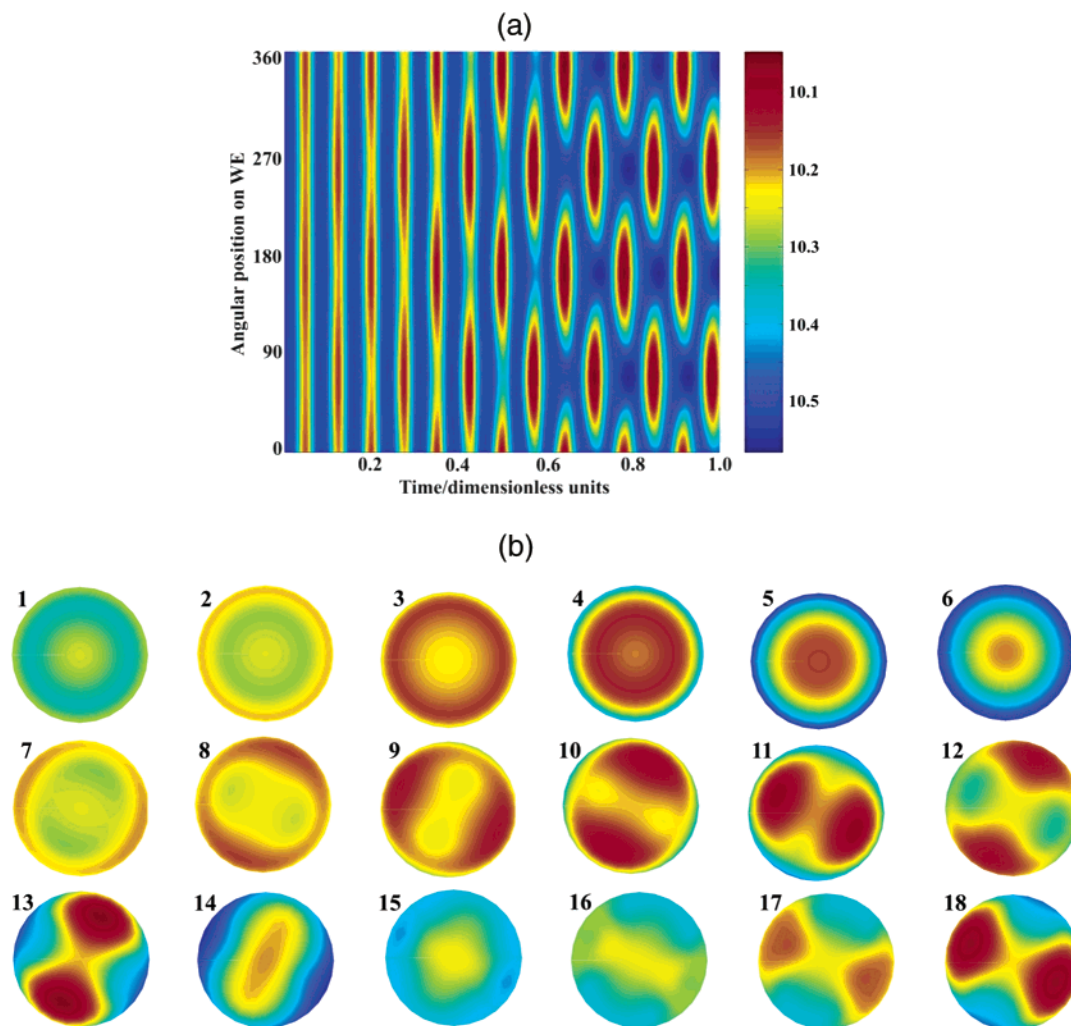


**Figure 3.** Transition from periodic oscillations to second-mode antiphase oscillations. With respect to Figure 2, the following parameters are different:  $\epsilon = 2.58 \times 10^{-2}$ ,  $\sigma^* = 0.362$ , and  $(h/\rho_{\text{CE}}) = 0.628$ . (a) The potential drop across the double layer as a function of angular position on the disk at  $\rho = 0.5\rho_{\text{WE}}$  and time. The color bar shows the coding of the dimensionless electrode potential: blue represents passive and red, active. (b) Snapshots of the potential on the disk working electrode at different times. First row, transient radially symmetric oscillations; second row, transition; and third row, half of a period of the asymptotic dynamics (second-mode antiphase oscillations).

boundary conditions in the plane of the WE.<sup>3,4,33,36</sup> Rather, it exhibits a radial dependence that can be illustrated recalling that the effective electrolyte resistance close to the edge of an electrode, which is embedded into an insulator, is smaller than that in the center of the disk.<sup>42</sup> Thus, viewing the electrode as being composed of infinitely many individual oscillators, the corresponding equations describing the homogeneous dynamics would differ in the value of the cell resistance  $R$ , depending on their radial position. Those with the larger  $R$  tend to be more active. Thus, on disk electrodes, the edge favors the passive state and the center the active one. This trend can be seen in the snapshots of Figure 2b. A radial profile taken along the symmetry axis of the snapshot is not symmetric with respect to the center of the disk. Rather, in the active half the most active part is located about a third toward the center, whereas in the passive half the most passive part coincides with the edge of the disk (Figure 2c). This characteristic is also found in all the remaining examples with the exception of Figure 8.

**3.2. Second-Mode Antiphase Oscillations.** In a different and smaller parameter range (compared to Figure 2,  $\epsilon$ ,  $\sigma$ , and  $\rho_{\text{CE}}$  of eq 10a,b were changed) the predicted long-term dynamics are symmetric with respect to a rotation by  $90^\circ$  and a shift in time by half an oscillation period. In Figure 3, the transition to

such a state from a homogeneous potential distribution and proton concentration is shown again in the same representations as presented in Figure 2. The homogeneous initial condition is unstable and oscillations first develop in which the radial symmetry is broken, but angularly the potential is nearly homogeneous (frames 1–6). This radial dependence of the electrode potential is again the result of the mixed boundary conditions in the plane of the WE. The first oscillations resemble the spatiotemporal behavior in the oscillatory region that was exclusively found if the RE was far away from the WE ( $z_{\text{RE}}$ ), i.e., with only weak global coupling. It resembles the experiments discussed by Kirkpatrick.<sup>46</sup>

A symmetry change in the azimuthal direction is only discernible after a few oscillatory cycles. The first half in Figure 3a and the second row in Figure 3b display this transition. The asymptotic dynamics is shown in the last half of Figure 3a and the last row in Figure 3b (these snapshots corresponding to half of the oscillation period). In contrast to the “base” antiphase oscillations, here every snapshot possesses two symmetry planes, i.e., it is invariant with respect to a rotation by  $180^\circ$ . Consequently, the dominating spatial mode in the angular direction possesses a wavenumber 2, as opposed to 1 for the base oscillation, an antiphase behavior being displayed between

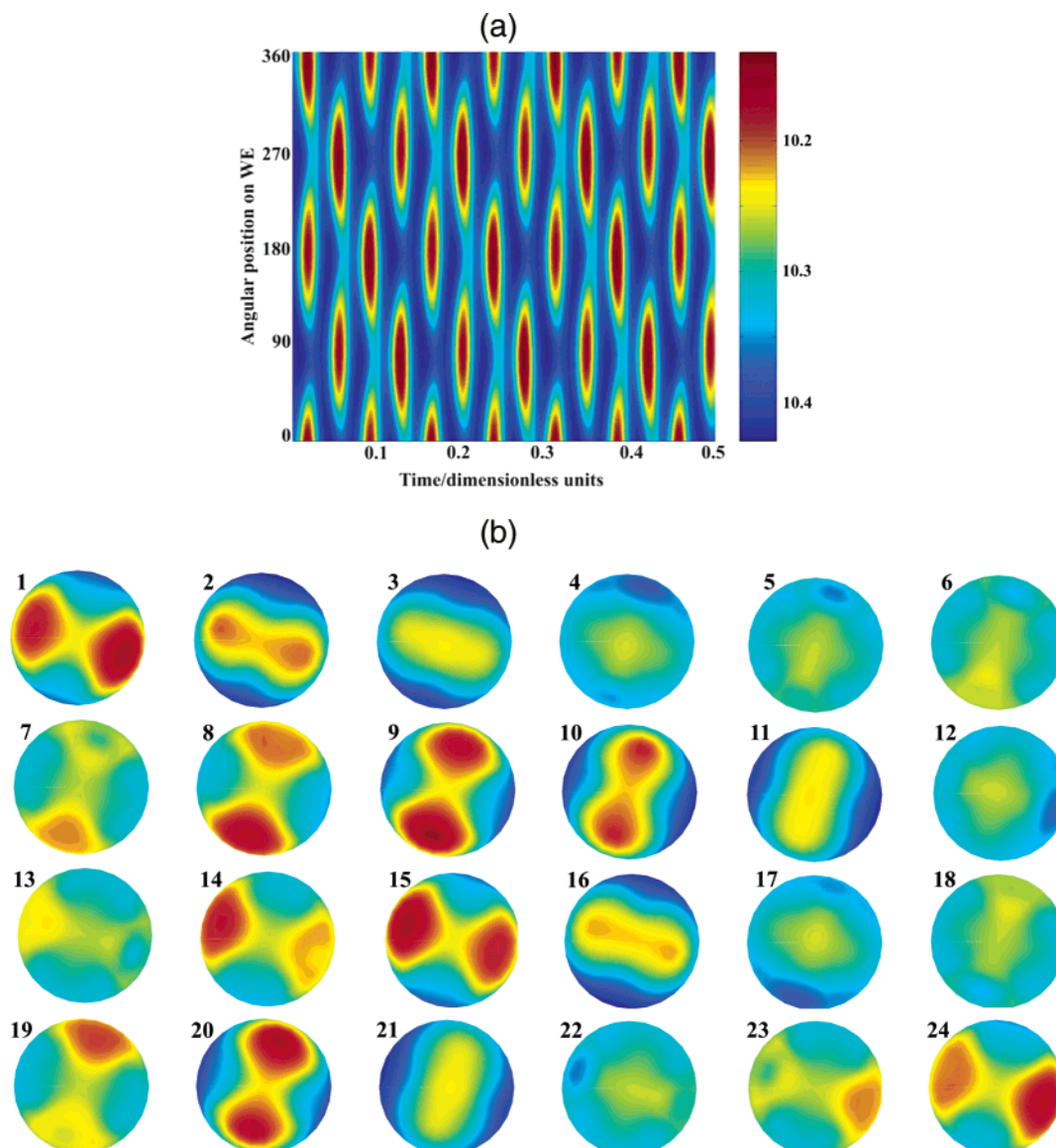


**Figure 4.** Spatiotemporal period doubling of the second-mode antiphase oscillations which occurs when lowering the conductivity from Figure 3 to 0.31. (a) The potential drop across the double layer as a function of angular position on the disk at  $\rho = 0.29\rho_{WE}$  and time. (b) Potential distribution on the disk working electrode at different times, covering one period of the oscillation.

locations that are phase shifted by  $90^\circ$ . The spatiotemporal behavior can thus be classified as a second-mode antiphase oscillation.

Let us have a closer look at the dynamics. In snapshot 13, Figure 3b, the potential pattern is composed of four regions, each covering approximately a quarter of the disk, two opposing ones being active and two passive, respectively. The total current corresponding to this situation has its maximum value. Then, gradually, the amplitude diminishes and the active regions contract along one of the two symmetry planes, reaching its minimum amplitude and extension (snapshot 15). The corresponding total current is thus also minimal. Then the active area expands along the second symmetry plane, perpendicular to the first one (frames 16–18). A corresponding evolution during the second half of the oscillation period brings the disk back to the initial stage. The total current is again periodic with a period half of a local oscillation.

These higher mode antiphase oscillations again were only found if the RE was sufficiently close to the WE, i.e., for a strong negative global coupling. Furthermore, when carrying out simulations with a thin ring electrode, antiphase oscillations

with a wavenumber 1 were obtained that very much resemble the temporal evolution shown in Figure 2a. A pattern with wavenumber two that would be close to the evolution of the angular position shown in Figure 3a was never obtained. This points to the fact that the second-mode antiphase oscillation again comes into existence because of the global coupling, and moreover, that it requires two spatial dimensions. Interestingly, a very similar phenomenon was observed experimentally during the electrodisolution of a *thick* iron ring electrode.<sup>21</sup>

### 3.3. Period-Doubled Second-Mode Antiphase Oscillations.

Different locations on the working electrode are coupled through the electric field within the electrolyte. The conductivity gives the strength of this migration coupling.<sup>3</sup> When decreasing the conductivity, starting from the second-mode antiphase oscillations, a spatiotemporal period doubling occurs. The resulting dynamics is shown in Figure 4. In the maximum amplitude state, the pattern shows two opposite active regions, each covering a quarter of the electrode, as in Figure 3. However, in contrast to the latter case, one-quarter is more active than the other one. Thus, every snapshot shown in Figure 4b has only one plane of symmetry, which rotates clockwise by  $90^\circ$  every quarter of

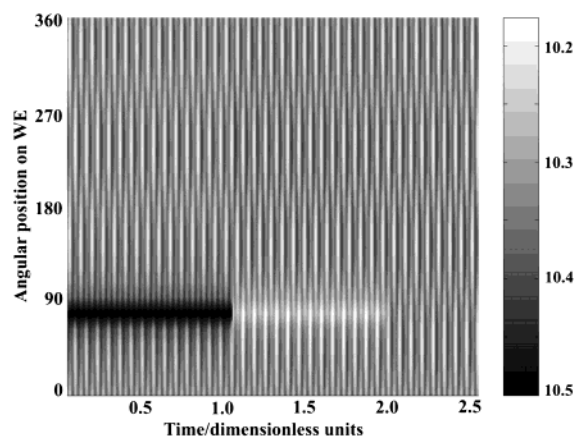


**Figure 5.** The effect of a constant perturbation on the second-mode antiphase oscillation from Figure 3. A potential value of  $-10.5$  was imposed on the disk at the location ( $\rho = 0.25\rho_{WE}$ ;  $\theta = 75^\circ$ ) between  $t = 0$  and  $t = 1$ . Plotted is the potential drop across the double layer as a function of angular position on the disk at  $\rho = 0.25\rho_{WE}$  and time. Black represents passive and white active.

a complete oscillation period. This results in local time series that are period-doubled with respect to those of the symmetric second-mode antiphase oscillations. The global current, in contrast, still oscillates with an unchanged period, which is now, consequently, only a fourth of the period of the spatiotemporal dynamics.

**3.4. Stability of the Second-Mode Antiphase Oscillations with Respect to Perturbations.** To test for the robustness of the second-mode antiphase oscillation, the response of the dynamics on different perturbations was studied.

*Constant Perturbation.* Figure 5 displays the response of the potential upon a local perturbation as a function of time and angular position for an intermediate radius on the disk. The perturbation was imposed at this intermediate value of  $\rho$  and an angle of about  $90^\circ$ . It was realized by fixing the potential at a value more negative than the other regions on the disk for one dimensionless time unit. At  $t = 1$ , the perturbation was lifted and thus the potential distribution was again free to adjust over the entire electrode. From Figure 5, it can be seen that

- The perturbation does not significantly distort the pattern at other locations. Due to the synchronizing nonlocal migration coupling, the potential value at neighboring positions is shifted to slightly more negative values compared to the unperturbed case. Further away from the perturbation point, the impact of the perturbation is minimal.

- After the perturbation is lifted, the system possesses a memory to the former constraint. The potential at the formerly perturbed location oscillates around a value that is more positive than its average in the unperturbed state for about 10 oscillations without any discernible further change. Only after a time which is comparable to the perturbation duration does the perturbed location return to the unperturbed dynamics. The transient ends suddenly, the system being indistinguishable from the asymptotic dynamics of the unperturbed state.

*Periodic Perturbation.* Let us next consider the response of the second-mode antiphase oscillations to a local periodic perturbation of the electrode potential. The perturbation frequency and the frequency of the pattern were incommensurate. The result is shown in Figure 6. Figure 6a,b display the azimuthal spatiotemporal evolution for the value of the radial coordinate at which the perturbation was applied. The perturbation was switched on at about 0.5 dimensionless time units and

turned off again at approximately 4.5 time units. As long as the perturbation is switched on, the second-mode antiphase oscillation prevails; the pattern is, however, considerably disturbed at the periodically forced location. Interestingly, after switching off the perturbation, the original dynamics does not recover but turns into a rotating pulse. Figure 6c shows the total current as a function of time. The two arrows indicate the start and end of the perturbation. The final constant value of the current corresponds to the rotating pulse, i.e., a region with constant amplitude and shape that propagates with constant velocity around the disk.

Obviously, the second-mode antiphase oscillations and the rotating pulse coexist at the chosen set of parameter values. Upon local periodic perturbations, the second-mode antiphase oscillations are less stable than the rotating pulse. The rotating pulse forms in this sense a more robust pattern.

**3.5. Mixed-Mode Antiphase Oscillations.** Yet another manifestation of antiphase behavior, obtained in a different region of parameter space, is displayed in Figure 7. The spatiotemporal dynamics is a variant of the base antiphase oscillation insofar as the disk is roughly divided in two halves with opposite behavior. Whenever half of the disk becomes more active the other half becomes more passive and vice versa. However, the amplitudes of individual oscillations vary drastically: a full oscillation period consists of several low- and high-amplitude antiphase oscillations. This gives rise to a time series of the global current that strongly resembles so-called “mixed-mode oscillations” (cf. Figure 7c,d).

To obtain a clearer picture how the spatial pattern evolves during one period of the total current, consider the snapshots displayed in Figure 7b. Frame 1 depicts a situation in which the upper half of the electrode is active; this corresponds to the maximum of the total current, denoted with 1 in Figure 7c. The amplitude decreases, and then the low-amplitude active area moves very fast to the opposite part of the disk, where the amplitude increases again (frames 1–5). The current attains a local minimum value (frame 3) and then reaches a local maximum of nearly the same amplitude as in point 1 (frame 5). This part of the evolution is similar to the antiphase oscillations. The two peaks of the total current are different as the extension and amplitude of the active area are slightly different for regions 1 and 5. Consequently, the activity decreases again, and the low-amplitude active region moves fast to the opposite part (frames 6–8). Then a slow evolution starts during which a weakly active region oscillates between the two parts of the electrode. This behavior corresponds to the low-amplitude peaks in the total current (frames 7–10). Gradually, the amplitude of these oscillations increases, until the same value as that in the initial frame is reached (frame 12). Since here the number of small amplitude oscillations is odd, in state 12 the active region is on the opposite side of the disk with respect to the initial frame 1. Thus, a full oscillation corresponds to two complete periods of the total current.

Changing the applied voltage, the number of small amplitude oscillations is modified. Figure 7d displays a time series of the total current for  $V_{apl} = -9.874$ ; compared to Figure 7c, the number of small amplitude oscillations increased. Furthermore, the dynamics becomes slightly irregular.

There are many experimental examples of electrochemical mixed mode oscillations, see e.g., the review papers in refs 2 and 3. They are generally interpreted in terms of a complex homogeneous dynamics which would require at least three variables.<sup>3</sup> Our results demonstrate that the mixed-mode char-

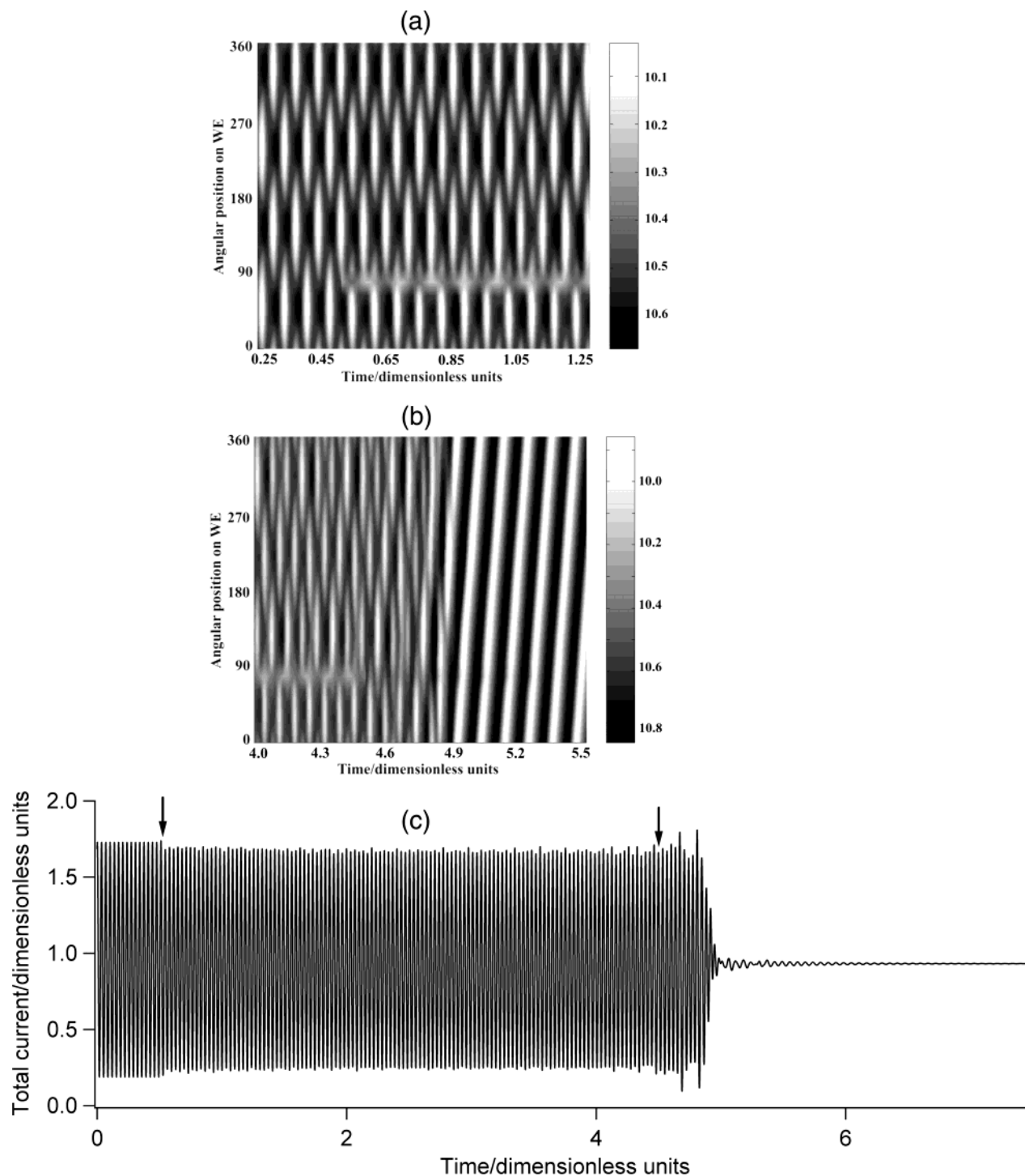


**Figure 6.** The effect of a periodic perturbation on the second-mode antiphase oscillation from Figure 3: transition to a rotating pulse. A potential value of  $-10.311 + 0.097 \sin\left(\frac{2\pi\nu_0}{\sqrt{2}}\right)$  with  $\nu_0 = 14.705$  was imposed on the disk at the location ( $\rho = 0.5625\rho_{WE}$ ;  $\theta = 75^\circ$ ) between 0.5 and 4.5 time units, where  $\nu_0$  is the local frequency of the unperturbed oscillation. Shown is the potential drop across the double layer as a function of angular position on the disk at  $\rho = 0.5625\rho_{WE}$  and time (a) between  $t = 0.25$  and  $t = 1.25$  and (b) between  $t = 4$  and  $t = 5.5$ . Black represents passive and white active. (c) Total current; the arrows mark the times at which the perturbation was switched on and off, respectively.

acter of the oscillations may also be a consequence of the spatial extension of the system.

**3.6. Rotation of a Complex Breathing Active Region.** The last example we consider here is an example in which the spatial coherence is less pronounced. Roughly, the spatiotemporal pattern consists of an antiphase-like division of the electrode, whereby, however, the active region expands and contracts mainly in the angular direction rather than oscillating between the two halves of the electrode. Superimposed on this breathing

motion is a slow clockwise rotation. The rotational motion is hard to recognize from the series of snapshots, but it is obvious in Figure 8a, where the angular evolution of the potential at a given radial position is shown. Furthermore, as evident from the total current (Figure 8c), the dynamics has a period-two character. Again, this feature can be hardly seen in the spatiotemporal evolutions (Figure 8a,b).

To obtain a better picture of the spatial motion, let us consider in more detail Figure 8b, where the potential on the disk at



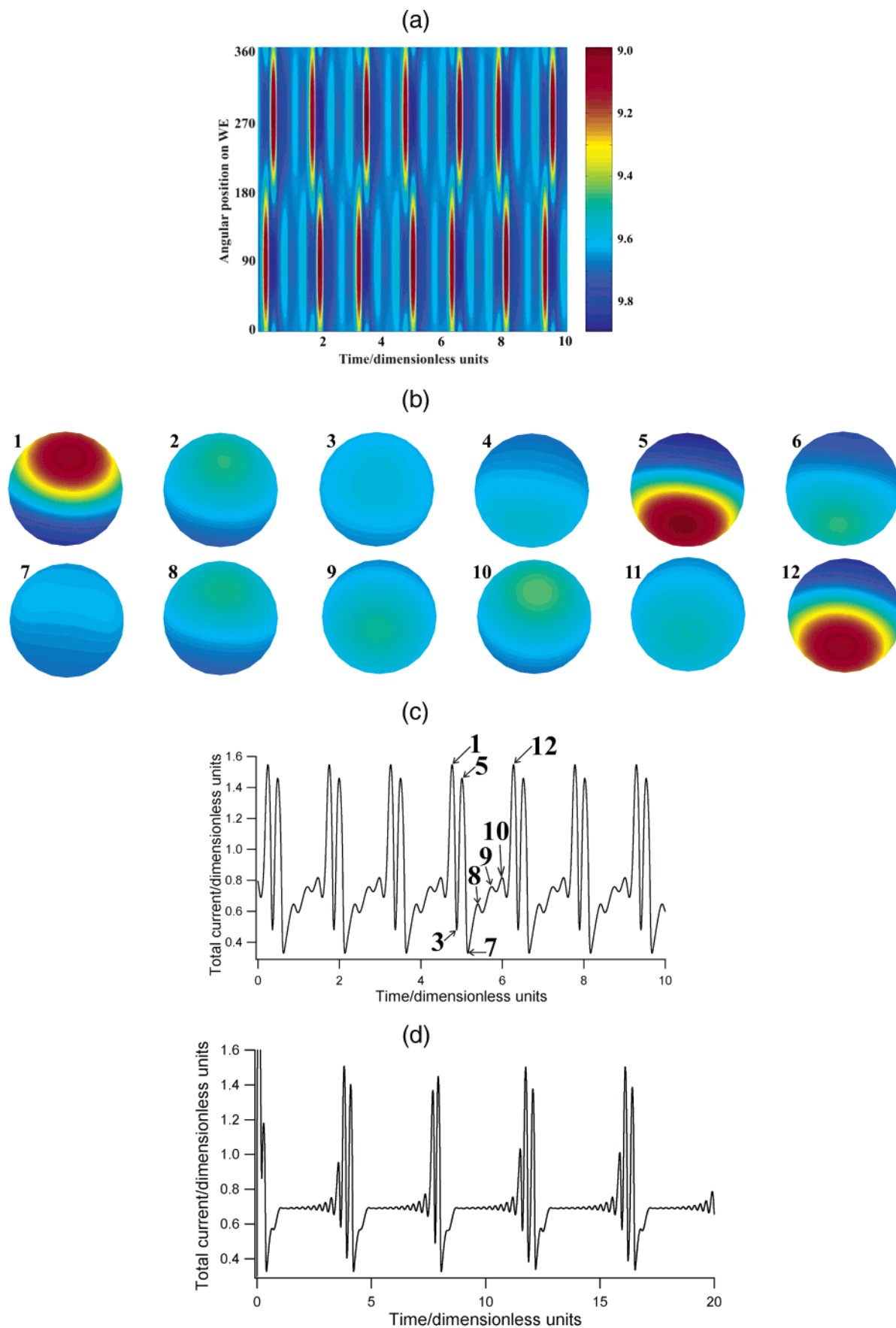


**Figure 7.** Mixed-mode antiphase oscillations. Parameter values:  $\epsilon = 2.58 \times 10^{-2}$ ,  $\sigma^* = 0.517$ ,  $\gamma = 1.033$ ,  $V_{\text{apl}} = -9.853$ ,  $\alpha = 6.46$ ,  $F_1 = 9.856$ ,  $F_2 = 2.321$ ,  $(\rho_{\text{WE}}/\rho_{\text{CE}}) = 0.8$ ,  $(h/\rho_{\text{CE}}) = 0.785$ , and  $z_{\text{RE}} = 0.9$ . (a) Potential drop across the double layer as a function of angular position on the disk at  $\rho = 0.5\rho_{\text{WE}}$  and time. (b) Potential distribution on the disk working electrode at different times, corresponding to half a period of the dynamics. (c) Total current, corresponding to (a) and (b). Values in (b) and (c) correspond to the same instants in time. (d) Total current for  $V_{\text{apl}} = -9.874$ ; other parameters as are the same as those in (a–c).

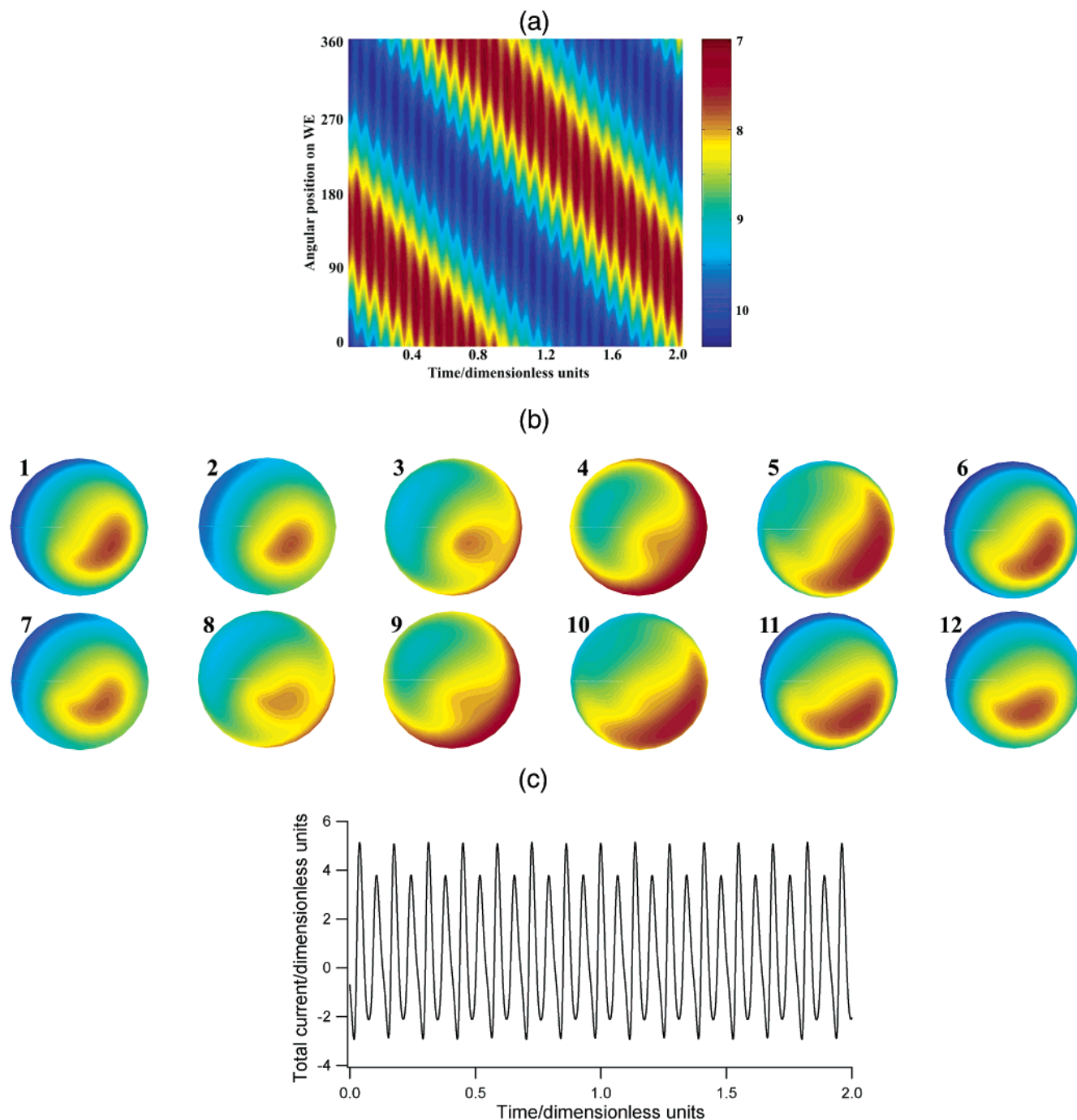


**Figure 8.** Rotation of a complex breathing active region. Parameter values:  $\sigma^* = 0.646$ ,  $\gamma = 25.846$ ,  $V_{\text{apl}} = -8.705$ , and  $(h/\rho_{\text{CE}}) = 0.162$ . The other parameter values are identical to those from Figure 7. (a) Potential drop across the double layer as a function of angular position on the disk at  $\rho = 0.5\rho_{\text{WE}}$  and time. (b) Potential distribution on the disk working electrode at different times. (c) Total current, corresponding to (a) and (b).

different times during a complete period of oscillation is shown. Initially, the potential distribution on the disk resembles one close to the current maximum of the antiphase oscillations: approximately half of the disk is more active and half is more passive. The active region contracts in radial direction while moving toward the edge and expanding in angular direction. Then, the motions reverse, i.e., contraction in the angular direction is accompanied by an expansion in the radial direction until the system reaches a state similar to the initial one. Due to the slow rotation, the active region is shifted by a small angle. This evolution corresponds to a large amplitude peak in the total current. Then a similar cycle, corresponding to the second half of the period, occurs, however, with somewhat smaller amplitudes.

#### 4. Conclusions

The presented simulations demonstrate how multifaceted spatiotemporal patterns which occur during the electrodisolution of metal disk electrodes with an active–passive region can be, if the RE is close to the WE, ranging from simple antiphase oscillations over second-mode antiphase oscillations and rotating, breathing active regions to mixed-mode oscillations.

The main driving force for the emergence of all these patterns is the negative feedback that exists in every electrochemical experiment under potentiostatic control when the distance between the WE and the RE is small compared to the distance between WE and CE. This feedback is proportional to a weighted average of the electrode potential; the closer a location

at the WE is to the RE, the stronger is its impact on the electrolyte potential at the RE.

From a more general point of view, the presented results are studies of pattern formation in activator–inhibitor reaction–diffusion type systems under a global constraint. In two-dimensional domains, such studies are still very rare.<sup>47–54</sup> Moreover, due to the different weight individual positions have, the global coupling realized in our model represents a general form of a global coupling. The impact of such asymmetric global couplings is thus far only poorly investigated.

The second-mode antiphase oscillations are examples of patterns that can apparently not be understood in the framework of a classic global coupling whose strength is proportional to the mean value of a variable. This makes a vital role of the asymmetric nature of our global coupling likely, and especially, it reveals that we are still far from a deeper understanding of the role that electrode geometries and the relative positions of the electrodes play for the spatial coupling when two-dimensional working electrodes are considered.

**Acknowledgment.** A. Bîrzu gratefully acknowledges support by a Humboldt Research Grant from the Alexander von Humboldt foundation. J. L. Hudson gratefully acknowledges support from the National Science Foundation.

## References and Notes

- Hudson, J. L.; Tsotsis, T. T. *Chem. Eng. Sci.* **1994**, *49*, 1493.
- Koper, M. T. M. In *Advances in Chemical Physics*; Prigogine, I., Rice, S. A., Eds.; Wiley: New York, 1996; Vol. 92.
- Krischer, K. In *Modern Aspects of Electrochemistry*; Conway, B. E., Bockris, J. O'M., White, R. E., Eds.; Kluwer Academic/Plenum Press: New York, 1999; Vol. 32.
- Flätgen, G.; Krischer, K.; Ertl, G. *J. Electroanal. Chem.* **1996**, *409*, 183.
- Hudson, J. L.; Tabora, J.; Krischer, K.; Kevrekidis, I. G. *Phys. Lett. A* **1993**, *179*, 355.
- Otterstedt, R. D.; Jaeger, N. I.; Plath, P. J. *Int. J. Bifurcation Chaos Appl. Sci. Eng.* **1994**, *4*, 1265.
- Otterstedt, R. D.; Jaeger, N. I.; Plath, P. J.; Hudson, J. L. *Chem. Eng. Sci.* **1999**, *54*, 1221.
- Otterstedt, R. D.; Plath, P. J.; Jaeger, N. I.; Sayer, J. C.; Hudson, J. L. *Chem. Eng. Sci.* **1996**, *51*, 1747.
- Otterstedt, R. D.; Plath, P. J.; Jaeger, N. I.; Hudson, J. L. *Phys. Rev. E* **1996**, *54*, 3744.
- Agladze, K.; Steinbock, O. *J. Phys. Chem. A* **2000**, *104*, 9816.
- Baba, R.; Shiomi, Y.; Nakabayashi, S. *Chem. Eng. Sci.* **2000**, *55*, 217.
- Grauel, P.; Varela, H.; Krischer, K. *Faraday Discuss.* **2001**, *120*, 165.
- Fei, Z.; Kelly, R. G.; Hudson, J. L. *J. Phys. Chem.* **1996**, *100*, 18986.
- Fei, Z.; Green, B. J.; Hudson, J. L. *J. Phys. Chem. B* **1999**, *103*, 2178.
- Green, B. J.; Hudson, J. L. *Phys. Rev. E* **2001**, *63*, 26214.
- Lev, O.; Sheintuch, M.; Pismen, L. M.; Yarnitzky, Ch. *Nature* **1988**, *336*, 458.
- Lev, O.; Sheintuch, M.; Yarnitsky, H.; Pismen, L. M. *Chem. Eng. Sci.* **1990**, *45*, 839.
- Lee, J.; Christoph, J.; Strasser, P.; Eiswirth, M.; Ertl, G. *J. Chem. Phys.* **2001**, *115*, 1485.
- Strasser, P.; Christoph, J.; Lin, W.; Eiswirth, M.; Hudson, J. L. *J. Phys. Chem.* **2000**, *104*, 1854.
- Nakabayashi, S.; Baba, R.; Shiomi, Y. *Chem. Phys. Lett.* **1998**, *287*, 632.
- Sayer, J. C.; Hudson, J. L. *Ind. Eng. Chem. Res.* **1995**, *34*, 3246.
- Varela, H.; Krischer, K. *Catal. Today* **2001**, *70*, 411.
- Flätgen, G.; Krischer, K. *J. Chem. Phys.* **1995**, *103*, 5428.
- Mazouz, N.; Krischer, K.; Flätgen, G.; Ertl, G. *J. Phys. Chem. B* **1997**, *101*, 2403.
- Mazouz, N.; Flätgen, G.; Krischer, K. *Phys. Rev. E* **1997**, *55*, 2260.
- Mazouz, N.; Flätgen, G.; Krischer, K.; Kevrekidis, I. G. *J. Electrochem. Soc.* **1998**, *145*, 2404.
- Mazouz, N.; Krischer, K. *J. Phys. Chem. B* **2000**, *104*, 6081.
- Karantonis, A.; Nakabayashi, S. *Electrochim. Acta* **2000**, *46*, 745.
- Bîrzu, A.; Green, B. J.; Otterstedt, R. D.; Jaeger, N. I.; Hudson, J. L. *Phys. Chem. Chem. Phys.* **2000**, *2*, 2715.
- Bîrzu, A.; Green, B. J.; Jaeger, N. I.; Hudson, J. L. *J. Electroanal. Chem.* **2001**, *504*, 126.
- Bîrzu, A.; Green, B. J.; Otterstedt, R. D.; Hudson, J. L.; Jaeger, N. I. *Z. Phys. Chem.* **2002**, *216*, 459.
- Christoph, J.; Otterstedt, R. D.; Eiswirth, M.; Jaeger, N. I.; Hudson, J. L. *J. Chem. Phys.* **1999**, *110*, 8614.
- Christoph, J.; Eiswirth, M. *Chaos* **2002**, *12*, 215.
- Plenge, F.; Rodin, P.; Schöll, E.; Krischer, K. *Phys. Rev. E* **2001**, *64*, 056229.
- Krischer, K. *J. Electroanal. Chem.* **2001**, *501*, 1.
- Krischer, K. In *Advances in Electrochemical Science and Engineering*; Alkire, R. C., Kolb, D. M., Eds.; VCH: Weinheim; **2003**, Vol. 8, 89.
- Grauel, P.; Christoph, J.; Flätgen, G.; Krischer, K. *J. Phys. Chem. B* **1998**, *102*, 10264.
- Grauel, P.; Krischer, K. *Phys. Chem. Chem. Phys.* **2001**, *3*, 2497.
- Krischer, K.; Mazouz, N.; Flätgen, G. *J. Phys. Chem. B* **2000**, *104*, 7545.
- Krischer, K.; Varela, H.; Bîrzu, A.; Plenge, F.; Bonnefont, A. *Electrochimica Acta* **2003**, in press. A negative Ohmic resistance can be realized experimentally with an active electronic device.
- Wang, Y.; Hudson, J. L.; Jaeger, N. I. *J. Electrochem. Soc.* **1990**, *137*, 485.
- Newman, J. *Electrochemical Systems*; Prentice-Hall: Englewood Cliffs, 1991.
- Koper, M. T. M.; Sluyters, J. H. *Electrochim. Acta* **1993**, *38*, 1535.
- Acton, F. S. *Numerical Methods That Work*; Harper&Row: New York, 1970.
- HSL 2002. *A Collection of Fortran Codes for Large Scale Scientific Computation*. <http://www.numerical.rl.ac.uk/hsl>.
- Pigeaud, A.; Kirkpatrick, H. B. *Corrosion* **1969**, *25*, 209.
- Schimansky-Geier, L.; Züllicke, C.; Schöll, E. *Z. Phys. B* **1991**, *84*, 433.
- Alekseev, A.; Bose, S.; Rodin, P.; Schöll, E. *Phys. Rev. E* **1998**, *57*, 2640.
- Bose, S.; Rodin, P.; Schöll, E. *Phys. Rev. E* **2000**, *62*, 1778.
- Falcke, M.; Engel, H. *Phys. Rev. E* **1997**, *56*, 635.
- Kuramoto, Y. *Int. J. Bifurcation Chaos Appl. Sci. Eng.* **1997**, *7*, 789.
- Lima, D.; Battogtokh, D.; Mikhailov, A.; Borckmans, P.; Dewel, G. *Europhys. Lett.* **1998**, *42*, 631.
- Rose, K.; Battogtokh, D.; Mikhailov, A.; Imbihl, R.; Engel, W.; Bradshaw, A. *Phys. Rev. Lett.* **1996**, *76*, 3582.
- Luss, D.; Marwaha, B. *Chaos* **2002**, *12*, 172.